Modification and Analysis of Integrated Enset (*Ensete ventricosum*) Processing Machine Components

B. Adugna[1], K. Purushottam Kolhe[2*], M. Gutu[1]

1- Department of Mechanical Engineering, School of Mechanical, Chemical and Materials Engineering at Adama Science and Technology University, Adama, Ethiopia
Department of Mechanical Engineering, Sinhgad College of Engineering, Vadgaon (BK.), 411041, SPPU Pune University, India
(*- Corresponding Author Email: kishorkolhe05@gmail.com)

https://doi.org/10.22067/jam.2025.91751.1334

Abstract

This research aimed to enhance the design and functionality of an integrated enset processing machine by focusing on key components such as the shaft, cylinder drum, breastplate, and drum blade. Existing enset processing machines suffer from inefficiencies due to component wear, mechanical breakdowns, and suboptimal design, leading to operational challenges. To address these issues, targeted design modifications were planned for the machine's components. The materials for these components were selected according to ASTM standards. The modified components were rigorously analyzed using the Finite Element Method in the Workbench module of ANSYS 2023 R1 software at Adama Science and Technology University, Adama, Ethiopia. The study reported maximum stresses of 120 MPa, 250 MPa, 400 MPa, and 260 MPa, and minimum stresses of 30 MPa, 70 MPa, 120 MPa, and 80 MPa for the shaft, cylinder drum, blade, and breastplate, respectively. Maximum deformations were found to be 0.15 mm, 0.3 mm, 0.55 mm, and 0.35 mm for these components, with a maximum safety factor of 15 for all. These results indicate that the modifications provide safe working conditions. The design ensures that the drum, drum blade, and breastplate possess sufficient rigidity to withstand operational forces, with minimal deformation (2.39×10^{-6} mm for the drum blade), remaining within a safety factor limit of 1.25. Additionally, the machine demonstrated excellent energy dissipation and vibrational response, indicating structural robustness.

Keywords: Breastplate, Cylinder drum, Deformation, Drum blade, Enset, Stress

Introduction

Processing *Ensete ventricosum*, commonly known as Enset, is essential to local economies and food production, serving as a major crop in Ethiopia and other parts of East Africa (Borrell *et al*., 2020). It has diverse uses in food processing, including its fibrous stalks and tubers, and plays a significant role in subsistence farming (Nabeshima, Moro, Campelo, Sant'Ana, & Clerici, 2020). The need for efficient processing equipment has driven the development of integrated machines aimed at increasing output and reducing labor intensity (Duflou *et al*., 2012; Jima, Kolhe, & Jiru, 2025). Components of enset processing machines, such as the shaft, cylinder drum, breastplate, and drum blade, are designed with standard mechanical properties and supported by relevant research literature (David Müzel, Bonhin, Guimarães, & Guidi, 2020).

Despite its significance, enset processing faces challenges due to the lack of advanced technology for efficient processing. Traditional manual methods are time-consuming and often yield inconsistent results. Mechanical devices intended to assist processing have not been widely adopted, mainly due to issues related to their efficiency, design, and integration into local agricultural practices. Attempts to mechanize corm grating have converted old manual methods into mechanical systems that reduce labor, time, and drudgery, helping communities address these challenges. However, integrated processing machines still suffer from inefficiencies, particularly in power consumption, component wear, and inconsistent quality of kocho and bulla products, which are limited by machine quality (Kudama, Tolera, & Gebeyehu, 2022). Literature reports that the shaft and power transmitters of decorticator and corm grater machines operate from a single power source (Workesa, Gebresenbet, Fanta, & Chaka, 2021). To ensure quality in decorticated pulpy tissue and minimize fiber damage, parameters including the breastplate's concave clearance, beater drum speed, and sheath feeding rate must be precisely adjusted, avoiding harm to fibers or residual pulpy sheath tissue (Deressa, Derese, & Dula, 2023). These challenges hinder the widespread adoption of such machines in rural communities where enset processing is a common practice.

To predict the mechanical behavior of enset processing machine components and refine the designs before physical prototyping, Finite Element Analysis (FEA) is employed (Jemghili, Ait Taleb, & Mansouri, 2023; Jima *et al*., 2025). This study focuses on technical aspects of modifying and analyzing integrated enset processing machines. FEA is a computational technique used to predict the behavior of materials and structures under various conditions such as stress, deformation, and movement (David Müzel *et al*., 2020). It divides complex structures into smaller elements and evaluates their performance, providing insights into real-world behavior. Key concepts in this analysis include stress analysis, which examines the internal forces acting on components, and fatigue analysis, which assesses material degradation from repeated stress. Additionally, understanding the material properties of the components is crucial for improving strength, flexibility, and durability (Hollaway, 2010). As noted, precise adjustment of parameters like breastplate concave clearance, drum speed, and sheath feeding rate is critical to maintain product quality without damaging fibers (Deressa *et al*., 2023).

Fabrication and assembly of enset machine components are facilitated by using materials without prior engineering property prediction, which can be improved by applying finite element analysis through computer-aided design (CAD) software (Digvijay & Kiran, 2015). Numerous numerical methods exist to solve complex physical problems with acceptable accuracy (Hamming, 2012). Among these, the finite element method is the most widely used in engineering. Its fundamental principle involves determining unknown node values using variational principal, as described by Xing, Qin, and Guo (2017), with the governing equation expressed in matrix form:

$$[C] \times [L] = [S] \qquad (1)$$

Where vector $[C]$ represents the unknown value of the quantity area at nodes, $[L]$ is the known load vector, and $[S]$ is the known constant matrix in the stress analysis.

The components of the integrated enset processing machine, such as shaft, beater drum, drum blade, breastplate, and power transmission elements are constructed from various engineering materials, designed to perform their functions without failure or damage to the fibers (Bekele, Lemu, & Jiru, 2022). Specific agricultural machinery parameters, such as operational load, force, torque, weight, torsion, dimension, and the shape of functional components were determined and used as input data in ANSYS software to optimize efficiency through the application of engineering principles (Chen *et al*., 2023).

Motion analysis and stress distribution were conducted using the finite element approach, confirming that all machine components operate without sustaining damage (Tezuka, 2006). For validation, finite element simulation of the model was employed (Szabó, Actis, & Rusk, 2021). The model was validated by comparing theoretical and simulation results for shear stress and angle of twist, both of which fell within acceptable limits. Key design considerations include the weight of the decorticator and grater cylinder, power requirements, pulley and belt design, shaft diameter, threshing torque, torsional moment, bearing design, and critical speed. It is important to note that even the most refined model remains an approximation of the real physical system (Szabó *et al*., 2021).

To ensure safe working conditions, the machine components will be manufactured with careful attention to design quality, feeding rate, operating speed, and the clearance between the beater and concave breastplate curve of the machines, all while maintaining cost effectiveness (Wang, Huang, & Yin, 2021). Additionally, any major issues that could compromise the machine's high safety factor, which may result in costly failures, will be addressed (Colledani *et al.*, 2014).

The objective of this study is to modify the design and functionality of an integrated enset processing machine by enhancing key components, including the shaft, cylinder drum, breastplate, and cylinder drum blade. These modifications aim to address common inefficiencies in existing machines, which are often affected by component wear, mechanical breakdowns, and poor design. These factors contribute to reduced operational efficiency. The proposed modifications focus on improving the machine's overall performance, durability, and safety.

This research specifically focuses on the redesign of the critical components of the integrated enset processing machine. The study entails the selection of materials according to ASTM standards for the components. It also involved simulating modified parts (Mahmood & Mohammed, 2022) using the Finite Element Method (FEM) in ANSYS Workbench 2023 R1. Furthermore, it includes a thorough analysis of the resulting mechanical behavior under operational conditions. The scope encompasses the evaluation of stresses, deformations, and the safety factor for each component, ensuring the machine's ability to withstand operating forces while minimizing operational risks.

The novelty of this study lies in the integration of advanced simulation techniques (FEM using ANSYS) to optimize the design of enset processing machine components. Unlike previous machines that suffer from frequent mechanical breakdowns and inefficiencies due to poor design and material choices, this research offers a solution by focusing on component-level modifications with a rigorous analytical approach. Another aspect of this study is the use of high safety factor values of 15 for all components and concentrates on minimizing deformation and maximizing energy dissipation and vibrational response. Additionally, the choice of materials based on ASTM standards and the thorough computational analysis represent an innovative approach to improving the overall functionality and durability of enset processing machines.

Materials and Methods

Materials

The design analysis focuses on the integration of mechanisms that enhance enset processing techniques, ensuring collaboration among the machine's components such as the shaft, beater drum, cylinder drum blade, and breastplate (Jima *et al.*, 2025). This involves coordinating the operating parts essential for the machine's functionality. The analysis emphasizes the importance of making critical design decisions that ensure the machine's structural stability, as highlighted by (Digvijay & Kiran, 2015). Key components such as the shaft, beater drum, drum blade, and breastplate are designed according to analytical formulas and standards to achieve this stability to guarantee efficiency in agricultural settings and lower economic losses for users (Zewdie, 2012).

Following the design phase, a computer-aided model using ANSYS 2023 R1 software was created. This model represents the computed and derived dimensions of the critical components, including the frame, shaft, cylinder drum, cylinder drum blade, and breastplate assembly. The design process integrates analytical tools, basic scientific principles, mathematics, and engineering software predictions to create an accurate product model. These methodologies are grounded in established engineering practices, as outlined by Silveira Velloso, Luis Gonçalves Costa, Rodrigues Magalhães, Lúcio Santos, and Tavares de Andrade (2018). The study conducted a detailed analysis of the integrated enset processing machine components to ensure a precise and reliable assessment of the system's performance.

Structure of sheath and corm enset

The enset is a perennial plant that grows between 4 and 11 meters tall and matures after 3-5 years for harvesting. It has corms and leaf sheaths overlapping to form the pseudo stem or trunk, which is important for food security in Ethiopia (Olango, Tesfaye, Catellani, & Pè, 2014). The corms are formed by extravagant tuber portions, including leaf sheaths, that are underneath and basal. When the enset plant reaches full maturity, its corms turn a vibrant orange color. To better understand the structure of the fibers in the corms, a study was conducted to examine the surface morphology of these fibers. A scanning electron microscope (SEM) (Philips XL-30 SEM, from the Netherlands) was used to observe the fine details of the surface. The SEM analysis revealed that fibers of the fully ripe, orange-colored corms have a somewhat fibrous texture, which is crucial for understanding the material properties of enset. This type of analysis helps researchers gain insight into the characteristics of the fibers, which may be important for applications such as processing and utilizing enset for various purposes, as noted by Huertas, Schmelzer, Hoehenwarter, Heyroth, and Heinz (2016).

In this case, the whole sheath was determined, where the overlapping leaf sheaths form the pseudo-stem containing broken, pulpy tissue and deformable fiber (Chen *et al.*, 2023). Also, to determine the weight of the samples of corm, an electronic balance with a sensitivity of 0.01 g was used (Bekele *et al.*, 2022). Three linear dimensions length (L), width (W), and thickness (T) were measured with a digital caliper (DC-515; Taiwan) with an accuracy of 0.01 mm to establish the average size of the cut corms (Ahangarnezhad, Najafi, & Jahanbakhshi, 2019).

To avoid polymer charging in electron beams, which can cause astigmatism (issues with focus and blurred images), fiber specimens were sputter-coated with a thin layer of gold-palladium before SEM examination. Next, the specimens were placed using carbon tabs on the SEM tube, which had a diameter of 12 mm by 12 mm with an accelerating voltage of 10.0 kV, fiber surfaces were scanned, and electron micrographs were captured. According to Bekele *et al.* (2022), in the exploration of the mechanical properties of enset fiber, the tensile strength of enset fiber is 513 ± 57.7 MPa and the tensile modulus is 26.7 ± 3 GPa with 1.92% elongation. These values highlight the fiber's strength, stiffness, and its ability to stretch under stress. Additionally, Yemataw *et al.* (2017) analyzed the morphological properties of enset by examining the recorded scans, providing insights into the structural characteristics of the fiber.

Design of components for an integrated enset processing machine

Physical and mechanical properties of the utilized materials

The input materials used for the fabrication of integrated enset processing machine components include stainless steel, mild steel, aluminum metals, and rubber. The physical and mechanical properties of the used material are presented in Table 1.

Table 1- Physical and mechanical properties of the materials based on the items provided

Type of material	Input materials component	Physical properties	Mechanical properties
Stainless steel	Cylinder drum	Dia. 25 cm (r = 12.5 cm), thickness = 2 mm, length = 45 cm for each, density (ρ) = 8000 kg m^{-3}	Durability, Poisson's Ratio (ν) = 0.3, Young's Modulus (E) = Yield Strength (σ_y) = 250 MPa
	Breastplate	Curvature = 17 cm, height = 45 cm, clearance 1-3 mm, length = 98 cm, density (ρ) = 8000 kg m^{-3}	Poisson's Ratio (ν) = 0.3, Young's Modulus (E) = Yield Strength (σ_y) = 250 MPa
	Blade	Length = 35 cm, thickness = 3 mm, density (ρ) = 8000 kg m^{-3}	Modulus (E) = Yield Strength (σ_y) = 250 MPa

Mild steel	Shafts	Dia. = 20 mm, length = 130 cm, density (ρ) = 7850 kg m^{-3}	Young's Modulus (E) = 210 GPa, Yield Strength (σy) = 250 MPa
	Angle	Width = 5 cm, length = thickness = 3 mm, density (ρ) = 7850 kg m^{-3}	Young's Modulus (E) = 210 GPa, Yield Strength (σy) = 250 MPa
Aluminum	Hopper and feeder	Thickness = 2 mm, lightweight, density (ρ) = 2700 kg m^{-3}	Poisson's Ratio (ν) = 0.33, Young's Modulus (E) = 70 GPa, Yield Strength (σy) = 120 MPa
	Conveyor	Thickness = 2 mm, lightweight, density (ρ) = 2700 kg m^{-3}	Poisson's Ratio (ν) = 0.33, Young’s Modulus (E) = 70 GPa, Yield Strength (σy) = 120 MPa
	Cover	Thickness = 2 mm, lightweight, density (ρ) = 2700 kg m^{-3}	Poisson's Ratio (ν) = 0.33, Young’s Modulus (E) = 70 GPa, Yield Strength (σy) = 120 MPa
	Pulley	Thickness = 4 mm, dia. = 20 cm, 12 cm, and 8 cm, lightweight, density (ρ) = 2700 kg m^{-3}	Poisson's Ratio (ν) = 0.33, Young’s Modulus (E) = 70 GPa, Yield Strength (σy) = 120 MPa
Rubber	Belts	Length = 180.5 cm, 140.65 cm, and 107.7 cm, top width of the belt = 13 mm, bottom width of the belt = 8 mm, thickness of the belt (t) = 8 mm, density = 1100-1200 kg m^{-3}	Elasticity, Durability, Flexibility, Poisson's Ratio (ν) = 0.49, Young's Modulus (E) = 0.01-0.1 GPa Yield Strength (σy) = 10-20 MPa

Design of the integrated enset processing machine

The disassembled overall components of the designed and developed Integrated Enset Processing (IEP) machine are schematically shown in Figure 1.A, and modified specifications of the functional processing parts and assembled diagram is illustrated in Figure 1.B.

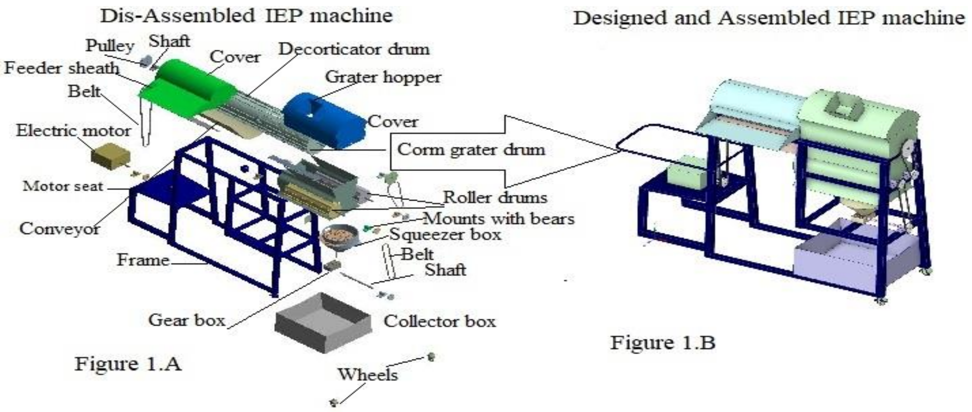
Dis-Assembled IEP machine

Designed and Assembled IEP machine

Figure 1.A

Figure 1.B

Fig. 1. Schematic illustration of the modified IEP machine components (A) disassembled, and (B) assembled

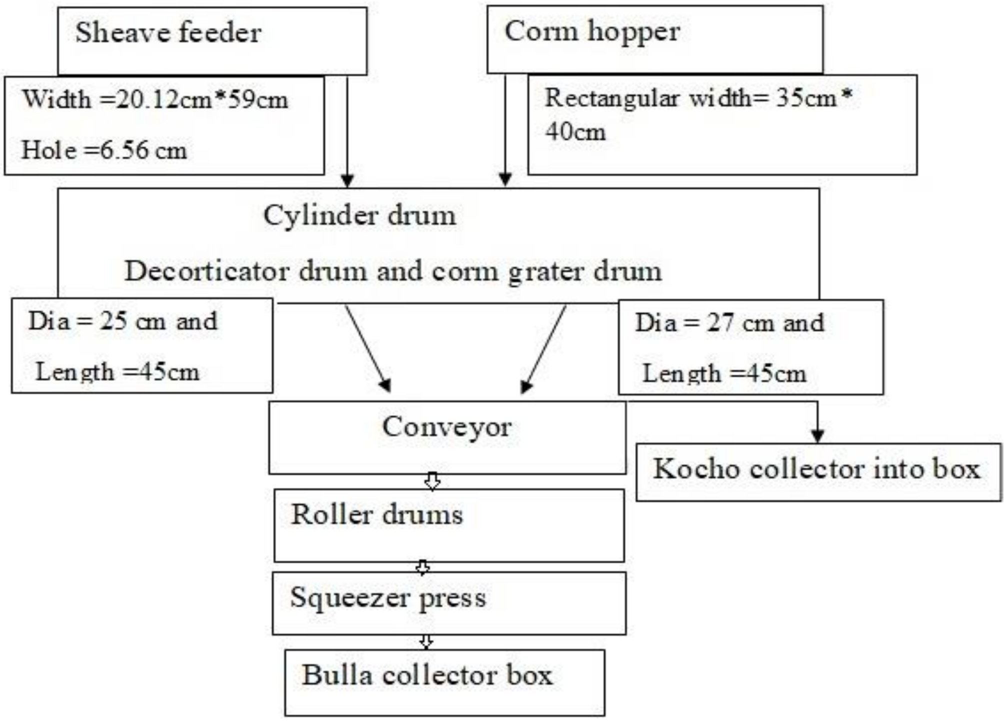

Fig. 2. Diagrammatic presentation of the device showing parts and dimensions of the integrated enset processing machine

Design calculations of the enset processing machine components

The machine requires an electric motor to operate the enset processing machine's parts, which involve two primary operations: decorticating the sheave (removing the outer layers of the enset plant) and grating the corm (grinding the inner part of the plant). Based on the data provided in Table 2, its power was determined as follows (Bello, Lamidi, & Oshinlaja, 2020):

$$Pd = \frac{2\pi N\tau}{60}\left(1-\frac{S}{100}\right) = \frac{2\pi\times N\times r\times(T1-T2)}{60}\left(1-\frac{S}{100}\right) = 1.166 \text{ kW} \quad (2)$$

where Pd is the output power required for both decorticate the sheave and corm grating in kW, τ is the twisting moment developed on the drum shaft (N m), N is the angular speed of the drum shaft (864 rpm), S is slippage (21.2%), $T1$ is tight side belt tension (221.57 N), $T2$ = slack side belt tension (90.07 N), $r = \frac{D2}{2}$, and $D2$ is the diameter of the pulley on the rotating shaft at the point of applying torque (0.20 m). τ = 0.10 m × (221.57 N − 90.07 N), V = 8.86 m s^{-1}, and slip on the smaller pulley at the first instance was considered as 2%.

The power source from the electric motor to operate the machine decorticating sheave and corm grating as of Figure (2) is well determined (Table 2). Therefore, the total sum of the power required to drive the decorticating unit (beater drum), and rollers to rotate the shaft of the squeeze press with its blade is determined. The output power recorded for grating the sheave and corm is 0.8875 kW, as determined by Equation (2). The total power (Pt) required for processing and overcoming friction can be determined as:

$$Pt = Pd + 0.3Pd = 1.52 \text{ kW} \quad (3)$$

$$Pd = (T1 - T2)V = 1.166 \text{ kW} \quad (4)$$

Where, Pt = total power required to drive the machine (1.52 kW), Pd = power required to drive the decorticating and grating unit and rollers unit (1.166 kW), and V = 8.86 m s^{-1}.

$$\tau = (T_1 - T_2)\frac{D_2}{2} = 13.15 \text{ N m} \quad (5)$$

$$T_1 = T_{max} - T_c \quad (6)$$

$$\frac{T1}{T2} = e^{\frac{\mu\alpha 1}{\sin\beta}} = T2 = \frac{T1}{e^{\mu\Theta}} = 90.7 \text{ N} \quad (7)$$

where, $T1$ = tight side belt tension

(221.57N), $T2$ = slack side belt tension (90.07N), and V = speed of belt (8.867m s^{-1}). μ = friction coefficient between contacting surfaces, $\alpha 1$, β , and θ = angles that affect the torque transmission efficiency in the system, e = the exponential constant used to model torque reductions due to friction and angular displacement, approximately (2.718), T_{max} = maximum torque applied in the system, T_c = torque loss or energy loss due to friction or inefficiencies, and $\frac{T1}{T2}$ is the ratio of the torques at two points in the system, indicating how torque changes through friction and other factors. The term $e^{\mu\Theta}$ shows how friction and angular displacement interact to reduce the torque at the second point.

According to Khurmi and Gupta (2019), the transmitted tension force T_1 is 221.57 N for shaft 1 with belt 1 system at 8.867 m s^{-1}; for shaft 2 opposite the rolling shaft 3, T_1 is 225.01 N at the belt speed of V = 8.69 m s^{-1}; and also shaft 4 with belt 3, T_1 is 228.145 N at speed of belt V = 8.52 m s^{-1}, derived from Equation (7). The torques on shaft 1, shaft 2, shaft 3, and shaft 4 would be determined by substituting these values in Equation (5), which were 10.42 N.m, 6.5 N.m, 6.5 N.m, and 6.17 N.m, respectively (refer to Table 2).

Rubber belts with a density of 1140 kg m^{-3} were utilized in this design because they are a common power transmission method in agricultural machines as recommended by ASME. This leads to an estimate of 0.096 kg m^{-1} for the rubber belt's mass per meter. T belt velocity as it passes over each pulley is calculated as:

$$V = \frac{\pi DN}{60}(1 - \frac{s}{100}) \qquad (8)$$

Since the active arc of contact is unknown, when inserting the value in Equation (8) the belt slip on the smaller pulley at the first instance was considered 2%. The velocity was estimated as 8.867 m s^{-1} over belt 1, 8.69 m s^{-1} over belt 2, and 8.52 m s^{-1} over belt 3.

Table 2- Parameters, equations, and results of modifications for the integrated enset processing machine

Parameter	Formula	Belt 1	Belt 2	Belt 3
Torque on a shaft (T)	$\tau = (T_1 - T_2)\frac{D_2}{2}$	13.15 Nm	12.98 Nm	7.92 Nm
Tension on the right side	$T_1 = T_{max} - T_c$	221.57 N	225.01 N	228.145 N
Tension on the slack side	$T2 = \frac{T1}{e^{\mu\Theta}}$	90.07 N	95.23 N	96.55 N
Diameter of the driven pulley (D_2)	20cm	20 cm	12 cm	12 cm
Center of distance (c)		65	45	35
Diameter of the drive pulley (D_2)		12 cm	20 cm	12 cm
Belt length	$l = 2C + 1.57(D1 + D2) + \frac{(D_2 - D_1)^2}{4C}$	180.5 cm	140.65 cm	107.7 cm
The maximum tension (T_{max})	$T_{max} = \sigma A$	235.20 N	235.20 N	235.20 N
The centrifugal tension (T_C)	$T_C = mv^2$	13.63 N	10.19 N	7.505 N
The mass of the belt (M)	$m = \rho A$	0.1733 + 18 kg	0.135 + 18 kg	0.10339 + 12 kg
Cross sectional area of a belt (A)	$A = (\frac{b - x}{2})t + xt$	0.0084m^2	0.0084m^2	0.0084m^2
Top width of the belt (b)		13	13	13
Bottom width of the belt (x)		8	8	8
Thickness of the belt (t)		8	8	8
The velocity of belt passing (V)	$V = \frac{\pi dN}{60}(1 - \frac{S}{100})$	8.867 m s^{-1}	$v = v\left(1 - \frac{S2}{100}\right) =$ 8.69 m s^{-1}	$v = v\ (1 - \frac{S3}{100})$ = 8.52 m s^{-1}

Maximum allowable stress of belt (σ)	$\frac{MY}{I} = \sigma$	28337.35 Pa	28337.35 Pa	28337.35 Pa
Density of belt material (rubber) (ρ)		1140 kg m^{-3}	1140 kg m^{-3}	1140 kg m^{-3}
Slip (S)		2%	1.8%	1.2%
Speed of the driving pulley (N)		864 rpm	1080 rpm	1080 rpm
angle of wrap on smaller pulley (α_1)	$\alpha1 = 180° - 2\sin^{-1}(\frac{D2 - D1}{2C})$	172.94°	180°	180°
Angle of wrap on larger pulley (α_2)	$\alpha2 = 180° + 2\sin^{-1}(\frac{D2 - D1}{2C})$	172.94°	180°	180°
Belt wedge angle (β)	40°	40°	40°	40°
Angle of contact at drive (θ_1)	$\theta1 = 180° + 2\alpha1 = 2\cos^{-1}(\frac{c}{2r})$	525.88°	540°	540°
Angle of contact driven (θ_2)	$\theta2 = 180° + 2\alpha2$	3.2648 rad	2.9638 rad	3.1426 rad
Coefficient of friction between pulleys and belt (μ)	$\mu = 0.54 - \frac{0.7}{2.4 + v}$	0.3	0.27	0.27
Groove angle	Standard (φ)	34°	34°	34°

The belt centrifugal tension (T_c) is determined as:

$$T_c = mv^2 \tag{9}$$

Accordingly, the centrifugal force at belt 1, belt 2, and belt 3 were 13. 63 N, 10.19 N, and 7.505 N, respectively.

Each belt's mass, cross-sectional area, maximum tension, and coefficient of friction between the belt and pulley are calculated using the following Equations (Bechtel, Vohra, Jacob, & Carlson, 2000):

$$T_{max} = \sigma A \tag{10}$$

$$m = \rho A \tag{11}$$

$$A = \left(\frac{b-x}{2}\right)t + x \times t \tag{12}$$

$$\mu = 0.54 - \frac{0.7}{2.4+v} \tag{13}$$

where: V = velocity of belt (m s^{-1}), T_c and T_{max} = the centrifugal and maximum tension of the belt (N); A = cross-sectional area of belt (mm^2); m = mass per unit length (0.096 kg m^{-1}) of belt; v = speed of belt (m s^{-1}); b = top width of the belt (mm); χ = bottom width of the belt (mm); d_1 = diameter of driving pulley (mm), N_1 = speed of the driving pulley (rpm); S = slip (%); σ = Maximum allowable stress of belt (28337.35pa) for coefficient of friction 0.35; t = thickness of the belt (mm); ρ = density of belt material (Rubber) (kg m^{-3}); T_2 = belt tension in slank side (N); μ = coefficient of friction between belt and pulley.

The power transmitted by the belt from the middle shaft pulley to the roller drum does not require a high load due to mixing only the soft materials of the pulpy tissue and grated corm is determined as (Khurmi & Gupta, 2019):

$$P = \tau \times \omega = 1.17 \text{ kW} \tag{14}$$

The rolling force in the mixer drum is as follows:

$$F_C = M_f \times S_f = 55.32 \text{ N} \tag{15}$$

where F_c is the rolling force of the design 55.32 N, M_f is the mass of roller, which is 36.88 N, and S_f is the factor of safety, which is 1.5, the diameter of the driver roller D is 19.5 cm with bar mild steel coated, r = 11.75 cm.

The torque transmitted to the roller mixer drum is calculated by (Yang, Zeng, Zhu, & An, 2017):

$$\tau = F \times r = 6.55 \text{ N m} \tag{16}$$

where τ = torque = 6.5 N m, F = force, and r = the radius of roller which is 11.75 cm.

Torsion and polar moment of inertia of shafts

The relationship between the torque (τ), shear stress (σ), and angle of twist (θ) in a circular shaft is determined from the general torsion equation as (De Felice & Sorrentino, 2019):

$$(\text{Ʈ}) = \frac{J \times G \times \theta}{L} \tag{17}$$

where: Ʈ = torque or twisting moment (N m), J = polar moment of inertia about the shaft axis (m^4), G = modulus of rigidity or shear modulus (Pa), θ = angle of twist (rad), and L =

length of the shaft (m).

The polar moment of inertia, *J*, represents the resistance of the shaft to twisting deformation. For a solid circular shaft, *J* is given by:

$$J = \frac{\pi D^4}{32} \qquad (18)$$

Where *d* is the diameter of the shaft.

The diameter of a solid shaft made of mild steel with little to no axial loading should be determined using the following formula, which comes from the American Society of Mechanical Engineering as:

$$\tau = \frac{\mathrm{HP} \times 4500}{2 \times \pi \times \mathrm{N}} \qquad (19)$$

Where the shaft is subjected to a twisting moment (or torque) only, the diameter of the shaft may be obtained by using the torsion equation:

$$\frac{\sigma}{J} = \frac{\tau}{r} \qquad (20)$$

Where: τ = twisting moment (or torque) acting upon the shaft, J = polar moment of inertia of the shaft about the axis of rotation, σ = torsional shear stress, and r = radius of the pulley.

According to Hosseini and Khadem (2009), the twisting moment acting on the shaft can be written as below:

$$\tau = \frac{\pi}{16} \times \mathrm{d}^3 \times \mathrm{fs} \qquad (21)$$

The machine weight applied at two places, W_1 and W_2, supported on two bearings “A” and “B”. Then it is apparent from the shear force diagram and bending moment well determined the correct shaft diameter to ensure satisfactory strength and rigidity that shaft is transmitting 2 hp power operating and loading conditions for 2 cm diameter. It reveals that 19.65 kg of both pully and belt weight supported by the shaft and the applied tension load weight on both sides, substituting the value in Equation (22):

$$\mathrm{Wn} = \frac{Mn \times l}{2} \qquad (22)$$

Where; *Mn* = applied weight of machine, *Wn* = applied load weight, *l* = length of shafts in cm.

Hence, the equivalent twisting moment, τ_{eq} is given by Equation (23) (Yakoob Pasha, Devi, & Maheswari, 2024):

$$\tau eq = \sqrt{\mathrm{W}^2 + \tau^2} \qquad (23)$$

$$= \sqrt{1277.38^{\,2} + 11946.13^2}$$

$$= 12014.229 \text{ kg. cm}$$

The equivalent twisting moment, when acting alone, produces the same shear stress as an actual twisting moment. Then both Equations (22) and (23) (Sinha & Turner, 2011) can be written as:

$$\tau \mathrm{eq} = \sqrt{\mathrm{W}^2 + \tau^2} = \frac{\pi}{16} \times \mathrm{d}^3 \times \mathrm{fs} \qquad (24)$$

Assuming permissible shear stress as 760 kg cm^{-2} steel shaft, the diameter of the shaft can be calculated as follows (Khurmi & Gupta, 2019):

$$d = \sqrt[3]{\frac{16(W^2 + \tau^2)}{\pi \times fs}}^{\,0.5} = \qquad (25)$$

$$\sqrt[3]{\frac{16(1{,}277.38^2 + 11{,}946.13^2)}{3.14 \times 760kg}}^{\,0.5} = 20 \text{ mm}$$

The linear velocity of leaf sheath for decorticating is:

$$v = \frac{\rho \omega n}{2\pi} = \frac{0.0079m \times 13.119m\, s^{-1} \times 18}{2 \times \pi} = \frac{0.364m}{s} \qquad (26)$$

Whereas, the pitch of the pulpy tissue extracted from the leaf sheath is:

$$p = \frac{2\pi v}{\omega n} \qquad (27)$$

Where: *P* = pitch of the tissue extracted from the leaf sheath (0.0079 m by assumption),

v = linear feeding speed of the leaf sheath to the decorticator (0.364 m s^{-1}), ω = angular velocity of the drum beater (864 rpm), n = number of blades on the cylinder (18), and θ = angle between two consecutive blades (20°), the power required for squeezing is:

$$\mathrm{p} = \frac{\mathrm{FR} \times \mathrm{t} \times \mathrm{b} \times \omega}{75} \times \eta \qquad (28)$$

Where: *P* is power requirement (1.2 hp), *FR* is fiber resistance (0.5 kgf cm^{-2}), *t* is blade thickness (3 mm), *b* is the effective width of the blade (13.5 cm), ω is the operational speed (2.7 m s^{-1}), and η is transmission efficiency (92%).

Accordingly, the corresponding torque generated by the squeezing press blade is calculated as (Lu, Li, Zhang, Fang, & Bin, 2023):

$$\text{Torque } (\tau) = \frac{Power}{Angular\ velocity} \quad (29)$$

$$= \frac{1,2\ hp}{\frac{2\pi\times12\times540}{60}} = 1.313 \text{ N.cm}$$

Power and load at worm and gear assembly

The worm gears are assembled on a 20 mm diameter shaft used for transmitting power at high-velocity ratios between non-intersecting shafts as shown in Figure 3. The load is applied at the end of the driving teeth when contact first forms and to be at the end of the driving teeth when contact ends (Mao, 2007).

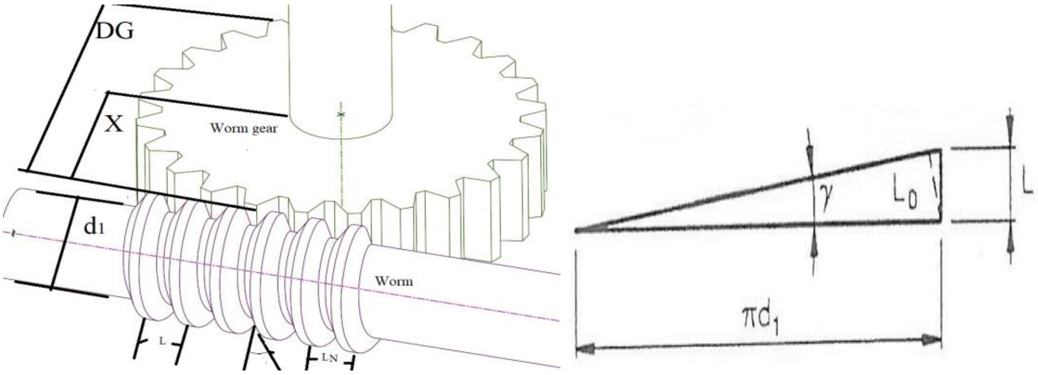

Fig. 3. Worm and gear when meshing

$$X = \frac{D_W + D_G}{2} \quad (30)$$

The pitch circle diameter of the worm (d_1) in terms of the center distance between the shafts can be written as (Radzevich, 2012):

$$d_1 = \frac{(x)^{0.875}}{1.416} \quad (31)$$

$$= \frac{(4.9)^{0.875}}{1.416} = 20\text{mm}$$

The lead "L" is the product of axial pitch and the number of starts and is determined mathematically as:

$$L = P_a \times n \quad (32)$$

Where, P_a = axial pitch (9.3 mm); and n = number of starts.

The lead angle between the tangent to the thread helix on the pitch cylinder and the plane normal to the axis of the worm is determined as (Vullo & Vullo, 2020):

$$\tan\lambda = \frac{\text{Lead of the worm}}{\text{Pitch circumference of the worm}} = \left(\frac{N_G}{N_W}\right)^{\frac{1}{3}} = \frac{L}{\pi d_1} = \frac{P_a\times n}{\pi D_W} = \frac{P_c\times n}{\pi d_1} = \frac{\pi m\times n}{\pi d_1} = \frac{m\times n}{d_1} \quad (33)$$

Where, N_G is the speed of the worm gear and N_W is the speed of the worm, axial pitch (P_a) = circular pitch (P_c), P_c = πm, m = module, and d_1 = pitch circle diameter of worm. The lead angle (λ) may vary from 9° to 45°. It has been shown that a lead angle less than 9° results in rapid wear, and the safe value for λ is 12.5° (Ambrus, Skadsem, & Mihai, 2018). For a compact design, the lead angle may be determined by equation (33).

The distance measured perpendicular to the threads between two corresponding points on two adjacent threads of the worm normal pitch is defined as Wu and Hsu (2014):

$$P_n = P_a \times \cos\lambda \quad (34)$$

The angle between the tangent to the thread helix on the pitch cylinder and the axis of the worm helix angle is determined as:

$$\text{Helix angle } (\alpha_w) \times \lambda = 90^\circ \quad (35)$$

Where, 90° is the shaft angle.

The ratio of the speed of the worm (N_w) in rpm to the speed of the worm gear (N_G) in rpm is the velocity ratio, determined as:

$$V_R = \frac{N_W}{N_G} = \frac{P_c T_G}{L} = \frac{P_a T_G}{P_a L} = \frac{T_G}{n} \quad (36)$$

The linear velocity of the worm is:

$$V_W = \frac{L\times N_W}{60} = \frac{\pi\times D_G N_G}{60} \quad (37)$$

The pitch circle diameter of the worm gear is expressed as:

$$DG = m \times TG \quad (38)$$

Where, m = module, D_G = pitch circle diameter of the worm gear, T_G = the number of teeth on the worm gear (twice of transmission ratio), and *n* = number of starts of the worm.

$$V_R = \frac{N_G}{N_W} = \frac{\pi D_G}{L} = \frac{\pi m T_G}{L} \quad (39)$$

According to Lewis equation, the strength of worm gear teeth size that is safe to assume is:

$$W_T = (\sigma o\,.Cv)\; b.\pi\, m\,.y \quad (40)$$

$= (84 \times 0.93)\ 28 \times \pi \times 3 \times 0.107$ N = 2825 N

Where, W_T = permissible tangential tooth load or beam strength of gear tooth, σo = allowable static stress, value may be taken as 84 MPa for cast iron, *Cv* = velocity factor (0.64), *b* = face width (28mm), *m* = module (3 mm), *y* = tooth form factor or Lewis's factor.

The velocity factor is given by:

$$C_V = \frac{6}{6+V} \quad (41)$$

Where; *v* is the peripheral velocity of the worm gear in m s^{-1}.

The tooth form factor or Lewis's factor (*y*) may be obtained in Equation (42). Therefore, the peripheral velocity was calculated at 0.38 m s^{-1} by substituting the value in Equation (41):

$$Y = 0.124 - \frac{0.684}{T_G} \quad (42)$$

The dynamic tooth load on the worm gear is determined (Mohanraj *et al.*, 2021) as:

$$W_D = \frac{W_T}{C_V} = W_T\left(\frac{6+V}{6}\right) \quad (43)$$

Where, W_T = actual tangential load on the tooth.

The static tooth load or endurance strength of the tooth (*WS*) may also be obtained (Al-Omiri, Mahmoud, Rayyan, & Abu-Hammad, 2010) as:

$$WS = \sigma e.b\,\pi\, m.y \quad (44)$$

$= 168 \times 28 \times \pi \times 3 \times 0.107 = 6075$ N, where, σe is the flexural endurance limit.

Its value may be taken as 84 MPa for cast iron and 168 MPa for phosphor bronze gears.

$$W_W = D_G.b.K \quad (45)$$

Where, D_G = pitch circle diameter of the worm gear, 162 mm, *b* = face width of the worm gear, and *K* = load stress factor (also known as material combination factor).

The forces acting on worm gears that transmit power to the worm are determined as (Yeh & Wu, 2009):

Tangential force on the worm:

$$W_T = \frac{2\times \text{Torque on worm}}{\text{Pitch circle diameter of worm } D_W} \quad (46)$$

Axial force or thrust on the worm gear:

$$W_A = \frac{2\times \text{Torque on worm}}{\text{Pitch circle diameter of worm } D_G} = \frac{W_T}{\tan\lambda} \quad (47)$$

The tangential force (W_T) on the worm produces a twisting moment of magnitude ($W_T \times \frac{D_W}{2}$) and bends the worm in the horizontal plane (Murugan, 2020).

The axial force on the worm tends to move the worm axially, induces an axial load on the bearings, and bends the worm in a vertical plane with a bending moment of magnitude ($W_A \times \frac{D_W}{2}$).

Radial or separating force on the worm is (Mei *et al.*, 2022):

$$W_R = W_A \times \tan\lambda \quad (48)$$

Where, $\tan\lambda$ = radial or separating force on the worm gear known as permissible input power:

$$p = \frac{3650\times x^{(1.7)}}{VR+5} \quad (49)$$

$= \frac{3650\times 0.02^{1.7}}{4+5} = 0.524$ kW, where *VR* = Transmission ratio.

Since this power is more than the given power to be transmitted (1.1 kW), therefore the design is safe from heat dissipation point of view. The radial or separating force tends to force the worm and worm gear out of the mesh. This force also bends the worm in the vertical plane. The gearbox encompasses the transmission units' worm and worm gear shaft at one end, achieving a reduction of 4:1 at the gearbox. This results in a rotation speed of 270 rpm at the shaft of the rotary blade. Suitable nuts and bolts are used for fastening the gearbox to the main frame, which can be removed when repair and maintenance is required.

Design analysis of major modified components of IEPM

This section describes the flow chart diagram modification (Figure 4) of the Integrated Enset Processing Machine (IEPM), which operates by electric motors derived from the integrated enset processing method and their functional parts.

The principle feeding unit and mechanical operation system, through which the enset sheath is fed into the machine's inclined plate for scraping, has been improved (Jima *et al.*, 2025). Enhancements were made with a focus on economic efficiency by considering factors such as size, power, production capacity, material loss, and overall operational efficiency, while maintaining product quality. Subsequently, the functional IEPM was modified and optimized, with certain parts being approved for testing. Its performance was evaluated through experimental analysis. Following the analysis, field experiments were conducted and validated against standard benchmarks, and the results were documented and analyzed.

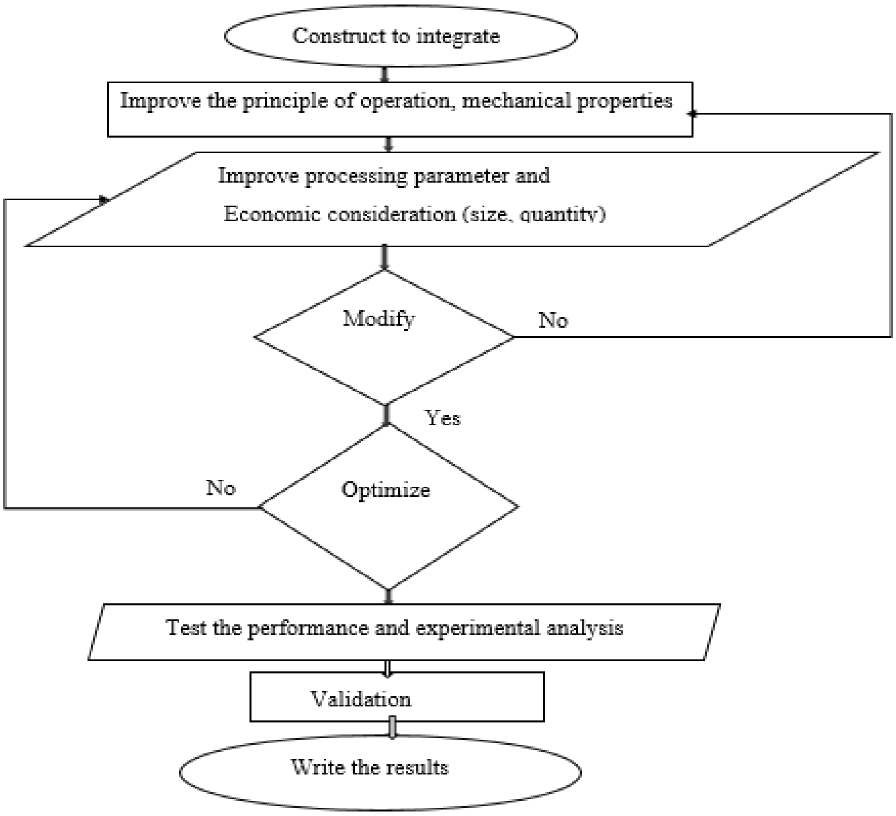

Fig.4. Flow chart diagram of the integrated enset processing machine (IEPM)

Finite element analysis of the IEPM components

A detailed computer-aided design (CAD) model of the integrated processing machine, illustrated in Figure 5, must be created to include components such as the shaft, beater drum, breastplate, and blade, with precision values calculated based on prior equations. The finite element method is utilized to analyze the distribution of shear stress, maximum deformation, and the safety factor of static structures. To ensure proper performance and assembly of the modified integrated enset processing machine, the weight of the machine components, and maximum allowable stress of belts with operational speed are considered.

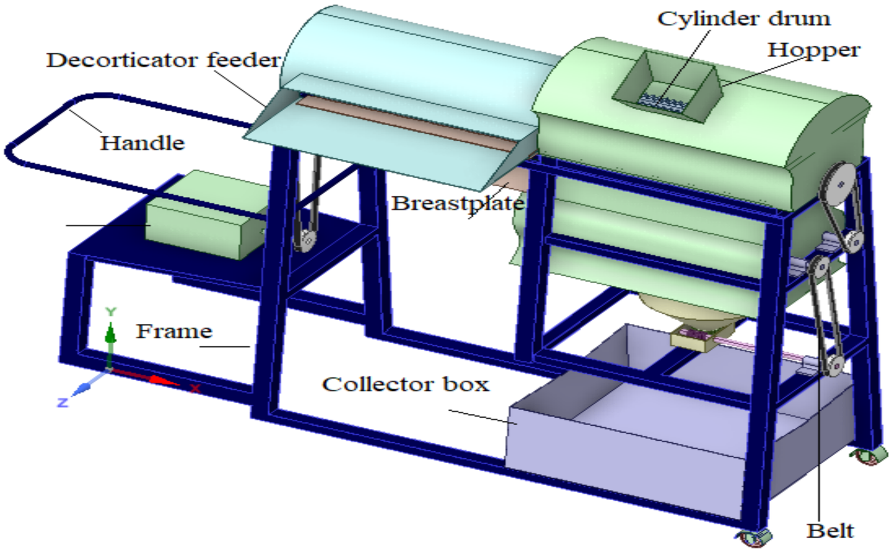

Fig. 5. The modified integrated enset processing machine

The majority of the integrated enset processing machine's components have a modulus of rigidity of about 77.2 GPa, constructed from stainless steel and Mild Steel. The mesh sizes used in the FEM analysis of each component vary as shown in Table 3. For a more thorough examination of their structural behavior, the mesh size for drum shaft, cylinder drum, drum blade, and breastplate as small as possible in contrast, a bigger mesh size for the main shaft. The grid convergence index values used in Equation (50) as shown in Table 3, the summary of materials' properties of components used for finite element simulations including discretization value, grid convergence ratio to determine real mesh size values as:

$$GCI = FS\frac{\varepsilon}{r^{p}-1}, \quad p = \frac{\ln|(f_{coarse}-f_{medium})/(f_{medium}-f_{fine})|}{\ln r} \tag{50}$$

where, ε = error, r = refine ratio, p = ordinary polynomial, and f = simulation results.

The simulation shows a low grid convergence index (GCI 0.66% at 21% refinement), indicating good accuracy in the results. The safety factor (S.F.) is 1.25, ensuring the shaft and other components operate within safe limits. The mesh refinement influences the accuracy of the simulation, with GCI values helping assess the need for further refinement in the model.

Static structural analysis (SSA)

The goal of static structural analysis (SSA) is to evaluate stress, strain, and deformation to ensure the machine could handle operational loads without failure on the integrated enset processing machine (Khodabakhshian & Emadi, 2015). The process involves assessing the machine's components (including the shaft, cylinder drum, breastplate, drum blade) under the application of forces or loads (Aygören & Türkdoğdu, 2024). The validation of the model is analyzed with the theoretical and simulation results of shear stress and angle of twist, are observed within the limits. The weight of the decorticator and grater cylinder, power, pulley design, belt design, shaft diameter, threshing torque, torsional moment, bearing design, and critical speed are considered. This analysis of the utilized materials, which may sustain higher stress values, highlights their significance. Interestingly, the drum shaft has an even greater modulus of 80 GPa, indicating increased rigidity in this crucial part. Commonly, for metallic materials with strong ductility, the Poisson ratios for the drum components and the breastplate are consistently 0.3 (Murugan, 2020). The belt, on the other hand (as shown in Table 2), has a noticeably greater Poisson ratio, indicating distinct material properties that would be more suited for flexibility.

A. Shafts

Under the analysis of static structure, the drum shaft has a modulus of even greater than 80 GPa (as depicted in Figure 5), indicating increased rigidity in this crucial part (Yang, Ma, Qin, Guan, & Xiong, 2022). This is common for metallic materials and is a sign of strong ductility. The Poisson ratios for the drum components are consistently 0.3 with a mesh size of 10 mm. The analysis of static structure results of the shafts shows a consistent stress distribution, indicating a well-balanced design with a diameter of 2 cm and a length of 130 cm. The belt tensions on either side of pulleys are *T1* = 221.5 N, *T2* = 90.07 N, *T3* = 225.01 N, and *T4* = 95.2 N, subject to a torque of 13.15 N m and a system's maximum tension of 235.20 N. The shaft is fixed in the middle (boundary condition). With the torque and belt forces operating within the system's design parameters and stability provided by the fixed midway, this configuration proposes a balanced tension distribution.

According to the analysis, the current shaft design is capable of withstanding operational loads without deforming (Bruyère, 1965; Jima *et al.*, 2025). The findings from the static structural analysis reveal a maximum stress of 120 MPa, a minimum stress of 30 MPa, a maximum deformation of 0.15 mm, and a minimum deformation of 0.03 mm.

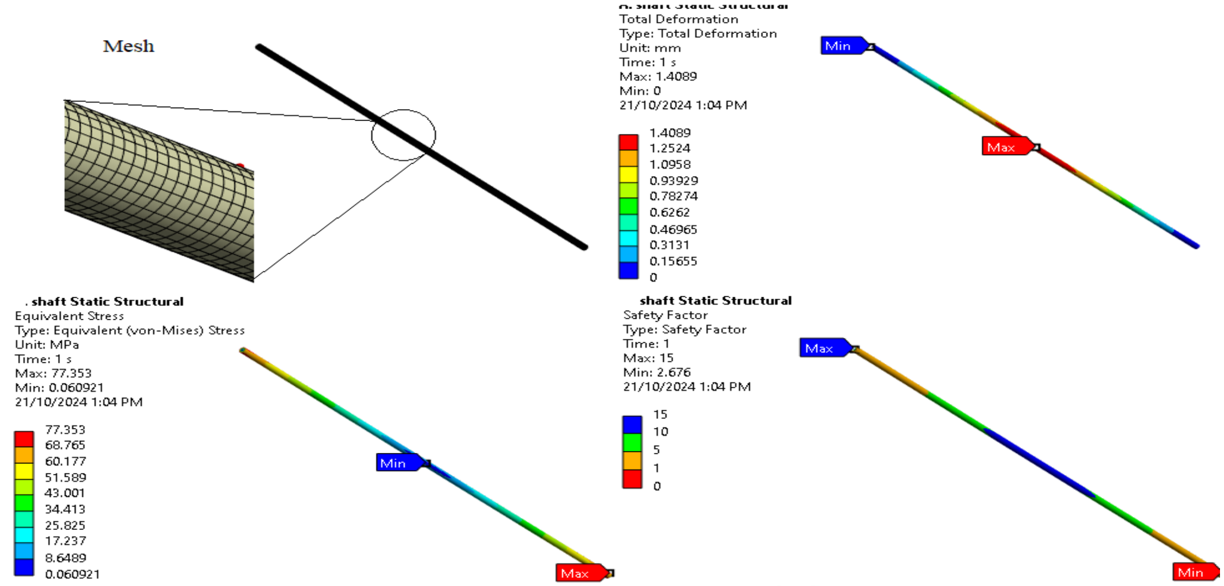

Fig. 5. Static structural analysis of shafts

B. Cylinder drum

The analysis of the static structure of the cylinder decorticator drum and grater drum with the properties of the same material is shown in Figure 6. The drum is mounted on the shaft, resulting in the following belt tensions on either side of the pulley: *T1* = 221.5 N, *T2* = 90.07 N, *T3* = 225.01 N, and *T4* = 95.2 N. With a consistent torque of 13.15 N m, the system reaches a maximum tension of 235.20 N. Additionally, the cylinder drum is fixed internally to the shaft (boundary condition). With the torque and belt forces operating within the system's design parameters and stability provided by the fixed, this configuration proposes a balanced tension distribution. The results of static drum cylinder structure reveal a minimum stress of 70 MPa, a maximum stress of 250 MPa, a maximum deformation of 0.3 mm, and a minimum deformation of 0.08 mm (Ambekar & Shinde, 2019). The analysis demonstrates that, under static load circumstances, the cylinder drum retains its structural integrity with little to no deformation. The results confirm the effectiveness of the drum's design (Carlson & McKean, 1955). Its performance could be further enhanced by reinforcement in high-stress areas, making it appropriate for heavy-duty applications (Sidhu & El-Sayegh, 2024). Discretizing a cylindrical drum into finite elements with a linear model allows for the analysis of optimal stiffness and damping properties for each element, as shown in Table 3.

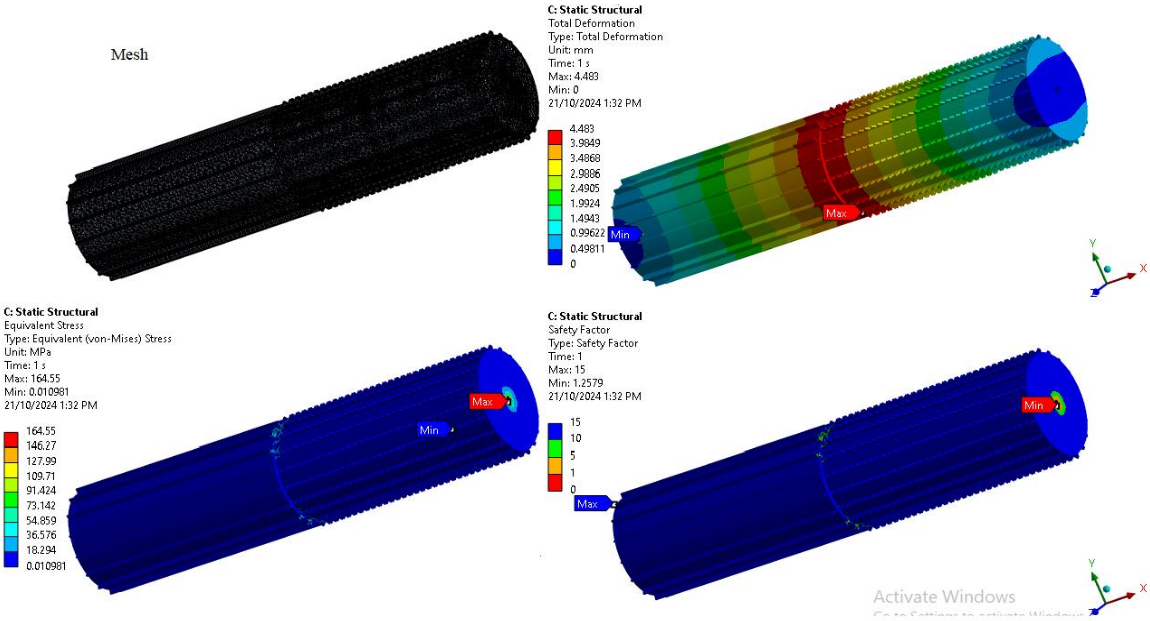

Fig. 6. Static structural analysis of the cylindrical drum

C. Cylindrical drum blade

The geometry of the cylindrical drum's blade is discretized into a finite element mesh using the data in Table 3. The element types were selected based on the nature of the generated boundary conditions, and certain nodes were fixed to represent supports or constraints (Upadhyay, Sonigra, & Daxini, 2021). The design should ensure that the mesh is fine enough in critical areas to capture stress gradients and deformation accurately. A total load of 235 N, the equal torque of both the shaft and the cylinder drum, is applied as a distributed load of 19.56 kg m^{-1} to the blade. This configuration influences the performance of the blade model and reflects its rotary dynamic design and intended cutting efficiency (Li *et al*., 2021). The cylinder drum blade static structural stability results are shown in Figure 7, with a minimum stress of 80 MPa, a maximum stress of 260 MPa, and 0.35 mm maximum deformation and 0.1 mm minimum deformation. The cylinder drum blade can withstand anticipated operating loads without experiencing appreciable deformation, according to the static structural study (Kordestani, Saif, Orchard, Razavi-Far, & Khorasani, 2019; O'Brien, Draper, & An, 2023). These results imply the robustness of the current drum design. However, to improve performance and lower manufacturing costs, lightweight composite materials should be investigated.

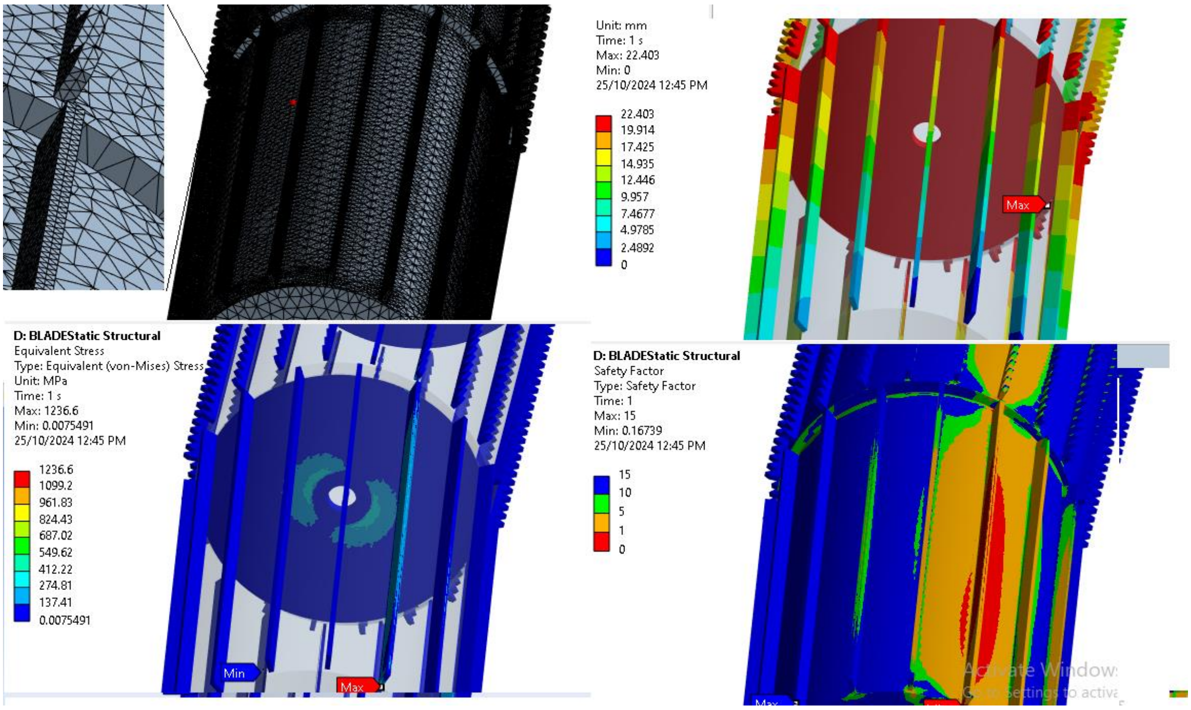

Fig. 7. Static structural analysis of the cylindrical drum's blade

D. Breastplate

Design of the breastplate model faithfully captures its ergonomic shape and protective coverage, with a frame beam supported from below (Jäger, 2023). The model indicates that the design successfully strikes a balance between mobility and protection. Curvature changes could improve comfort and use less material without sacrificing safety (Mansfield, Naddeo, Frohriep, & Vink, 2020). Discretizing the mesh into finite elements with linear elements reveals that each element possesses adequate stiffness and effectively resists the analyzed damping drums (Adamiec-Wójcik, Brzozowska, & Drąg, 2015; Lemos, 2007). The static structural analysis results of the breastplate, shown in Figure 8, identify possible failure locations through regions of significant stress concentration under the distributed static load of 235 N. The analysis reveals a maximum stress of 400 MPa and a minimum stress of 120 MPa, with corresponding maximum and minimum deformations of 0.55 mm and 0.15 mm, respectively, and a safety factor of 15 (Feng & Young, 2013). To improve the breastplate's durability and protective qualities, it is recommended to utilize advanced materials and reinforce areas expressing high stress, thereby ensuring improved performance in practical situations.

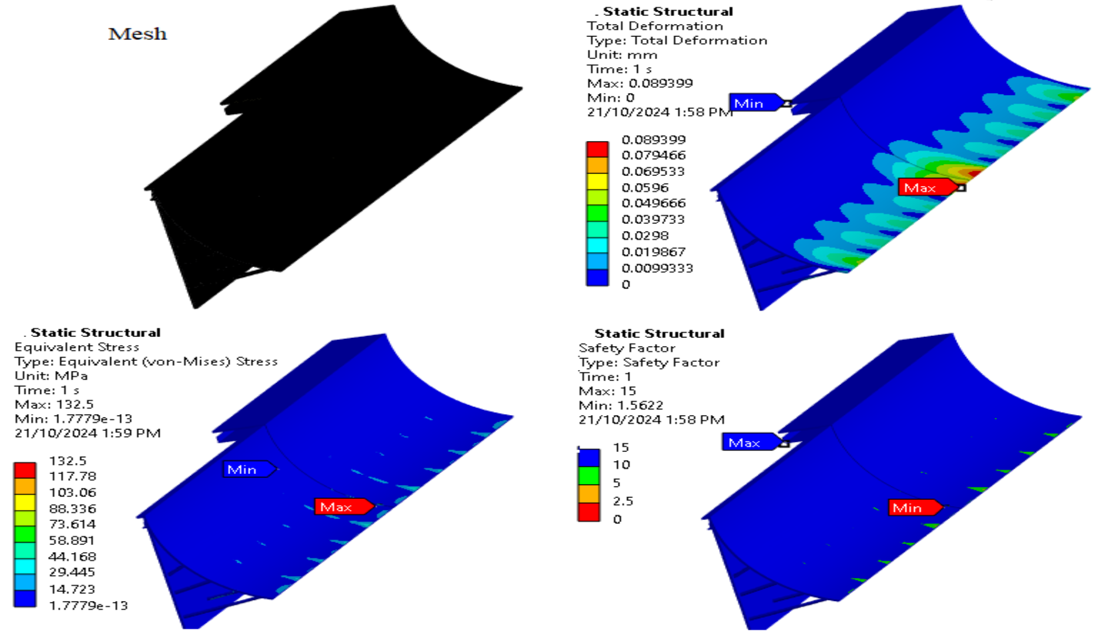

Fig. 8. Static structural analysis of the breastplate

Explicit dynamics structural analysis (EDSA) cylinder drum with breastplate

A computational method for analyzing the dynamic load condition of 942.78 N, using Explicit Dynamics Structural Analysis, determined the structural responses under time-dependent loads (Chopra, 2021). The analysis focuses on two main components: the cylinder drum, a rotating device used for processing materials, and the breastplate, a protective shell enhancing structural integrity through added support. Critical material parameters, including density, Poisson's ratio, and modulus of rigidity, sourced from Table 3, were incorporated to model mechanical behavior. Equation (51), derived from the analysis, proves valuable for machinery components involved in scraping the pulp from fiber cylinder drums interacting with breastplates, where rapid load fluctuations occur (Ham & Bathe, 2012). The study revealed diverse loading situations, such as beginning scenarios, such as initial conditions, tangential forces, and operating loads, to simulate realistic operational scenarios as:

$$F = m\frac{d^2s}{dt^2} + D\frac{ds}{dt} + RS \tag{51}$$

Where: F = external force vector, m = mass matrix (N), D = damping matrix, R = stiffness matrix, and S = displacement vector, d^2S/dt^2 = the acceleration vector, and ds/dt = the velocity vector. The maximum displacement calculated during dynamic loading of the drum under operational conditions is 1.196 mm. The stiffness of the drum is 1.86×10^8 N m^{-1}, and the stiffness of the breastplate is 1.07×10^8 N m^{-1}. The damping coefficient for the drum is 186,000.65 Ns m^{-1}, which dissipates energy over time. The external force vector value was 234.51 N. For each component of the cylinder drum and breastplate, the mass matrix can be calculated based on the density (ρ), volume (v), and mesh size.

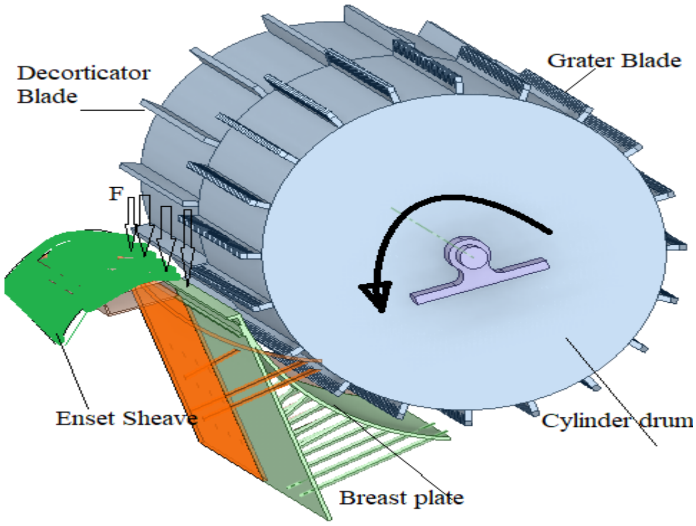

Fig. 9. Cylinder drum with breastplate

The cylinder drum and breastplate are structurally sound under the applied dynamic loads according to the study. Operational truthfulness is maintained by ensuring that the calculated maximum displacement remains within practical limits. Both components can sustain large loads without experiencing excessive deformation, according to the stiffness values. The damping properties imply efficient energy dissipation, reducing vibrations, and improving stability while in use.

Analyzing the stiff dynamics of a cylinder drum under applied load reveals a complex oscillatory behavior that is essential to evaluating the mechanical performance of the drum. The drum shows no displacement at the beginning (t = 0 seconds), suggesting a stable starting position. Severe displacement variations are seen in the data throughout time, concluding at about 2.39×10^{-6} mm at t = 0.82 seconds, indicating severe deformation under load.

Results and Discussion

The mass of the belt, its cross-sectional area, and the maximum tension of each belt are shown in Table 3. The mass of belts per unit length was 0.096 kg m^{-1}, the cross-sectional area of the belts was determined as 0.0084 m^{2}, and the coefficient of friction between pulleys and the belts was estimated to be 0.3. The analysis of the mechanical properties of integrated machine components reveals that the drum shaft, with a rigidity modulus of 80 GPa, along with the drums and other components at 77.2 GPa, exhibits strong resistance to deformation. The modulus of rigidity and the drums' modulus of stiffness is nevertheless quite high.

Table 3- Mechanical properties of the machine materials used for simulations

Model	**Modulus of rigidity (GPa)**	**Poisson ratio**	**Mesh size (mm)**	**No.E/t 1**	**No.E/t 2**	**No.E/t 3**	**V1**	**V2**	**V3**	**S.F.**	**GCI 21% (%)**	**GCI 32% (%)**
Drum shaft	80	0.27-0.3	10	70992	7344	612	77353019.79	76950604.06	101584956.4	1.25	0.66	30.82
Drums	77.2	0.3	3	279933	138011	76320	379958408.5	168617655.8	159769668	1.25	3.04	6.94

Decorticator blade	77.2	0.3	3.5	898820	499928	175817	20986878.4	19685794.1	15706624.73	1.25	3.76	8.57
Breastplate	77.2	0.3	3.5	187123	58438	12712	33610046.27	31808901.7	25821077.33	1.25	2.88	7.104
Belt	0.0003	0.45-0.5	2	7832	537	158	0.007174795	0.007147995	0.006294032	1.25	0.02	2.344
Frame	80	0.27-0.3	10	699523	240970	67420	597707.6887	597005.3962	518674.0509	1.25	0	3

Note: "No. E/t" values represent the number of elements per thickness for different parts, while V1, V2, and V3 represent the number of elements for different parts.

The correctness of the mesh and simulation results are indicated by the grid convergence index (GCI) values; higher percentages indicate more reliability, as shown in Table 3. The simulation records intricate reactions with a mesh size of 10, and the high No.E/t value of 70992 indicates significant stiffness. The design can safely bear expected loads, according to the safety factor (S.F.) of 1.25. The GCI values, which indicate good stability and performance, especially under complex geometrical configurations, are 0.66% for 21% and 30.82% for 32%.

For example, the decorticator blade drum displays a GCI of 3.76% at 21%, suggesting moderate reliability in its analysis and performance predictions. The No.E/t value of 279933 indicates strong stiffness in the major loading direction, while the mesh size of 3 offers sufficient information for simulations. Reliability during operation is indicated by the S.F. of 1.25. With performance improving as geometrical complexity grows, the GCI values of 3.04% (21%) and 6.94% (32%) show good design integrity. A Poisson ratio of 0.27 to 0.3 indicates moderate lateral expansion upon compression, making it suitable for various loads.

Consistency between components is ensured by the decorticator blade drum's 77.2 GPa stiffness modulus. A somewhat more in-depth investigation is possible with a mesh size of 3.5. The No.E/t numbers indicate different stiffness properties for different orientations, especially the first one at 898820. A significant reactivity to geometrical changes is implied by the GCI values of 3.76% and 8.57%, suggesting possible areas for structural modification. The safety factor stays at 1.25, showing constant reliability.

Additionally, the breastplate exhibits a homogeneous material selection with a modulus of stiffness of 77.2 GPa. It has enough information for simulations with a mesh size of 3.5, but its No.E/t value of 187123 suggests that it is slightly less rigid than the drums. Under operational settings, reliability is reinforced by the consistent safety factor of 1.25. GCI ratings of 7.104% and 2.88% demonstrate the breastplate's resilience to changing geometrical conditions without compromising structural integrity. The four shafts' mechanical characteristics and applicability for different applications are emphasized by the study results shown in Table 4.

Table 4- The shafts' mechanical properties based on the given parameters

Parameter	Shaft 1	Shaft 2	Shaft 3	Shaft 4
Weight (W)	19.65 kg	4 kg	4 kg	2 kg
Load (L)	235 N	221.5 N	225 N	228.2 N
Tangential Force($\boldsymbol{F_t}$)	131.5 N	234 N	-234 N	2825 N
Length (l)	130 cm	65 cm	65 cm	45 cm
Diameter (d)	20 cm	12 cm	12 cm	12 cm
Speed (RPM)	864	1080	1080	1080
Polar Moment of Inertia (J)	1.57×10^{-3} m^4	1.77×10^{-4} m^4	1.77×10^{-4} m^4	1.77×10^{-4} m^4
Modulus of Rigidity (G)	80 GPa	80 GPa	80 GPa	80 GPa
Power (P)	1.5 kW	1.17 kW	1.17 kW	1.117 kW
Torque ($\boldsymbol{\tau}$)	13.15 Nm	6.50 Nm	6.50 Nm	6.17 Nm

Torsion	1000 Nm	1000 Nm	1000 Nm	1000 Nm
Shear Force (F)	131.5 N	234 N	234 N	2825 N
Maximum Stress (σ_max)	16.73 MPa	55.67 MPa	55.67 MPa	49.27 MPa
Allowable Stress (σ_allow)	84 MPa	84 MPa	84 MPa	84 MPa
Safety Factor (SF)	5.02	1.51	1.51	1.71
Twist moment (θ)	1.67 degrees	1.13 degrees	1.13 degrees	1.01 degrees

Excellent resistance to torsional deformation is provided by shaft 1, which is the heaviest at 19.65 kg, bears a maximum load of 235 N, and has a polar moment of inertia of 1.57×10^{-3} m^4. However, the structural integrity of shafts 2 and 3, which weigh only 4 kg apiece and support loads of roughly 225 N, is called into question due to their higher maximum stress levels (55.67 MPa), which are close to their permitted limit of 84 MPa. Shaft 4 shows an abnormally high tangential force of 2825 N, suggesting possible design issues, even though it weighs only 2 kg. According to torque measurements, shaft 1 can withstand higher twisting forces (10.42 N m), but the others range. Also, this shaft can withstand twisting forces of up to 10.42 N m, whereas the others can withstand twisting forces between 6.17 and 6.50 N m. While shafts 2 and 3 have lower safety factors of about 1.51, shaft 1 likewise has a high safety factor of 5.02, demonstrating resilience under unforeseen pressures. Subsequently, the strength and longevity of shaft 1 make it perfect for high-load applications, but lighter shafts can be preferable in situations where weight is a concern but need close supervision to avoid failing under pressure. This analysis highlights how crucial it is to choose shaft designs according to particular operational requirements and safety considerations.

Several important interpretations that are necessary for analyzing the cylinder drum and breastplate's performance in an enset processing machine were obtained from the explicit dynamic structural analysis. Critical information systems performed in various operational cylinder drums can be obtained by analyzing dynamic and operational load conditions. With a torque of 10.42 N m at 864 rpm, the computed dynamic load of 942.78 N is obtained, demonstrating the strong rotating forces at work. On the other hand, the highest tension and centrifugal tension acting on the belt system are considered when determining the operational loads, which vary between 207.94 N and 220.64 N across three scenarios.

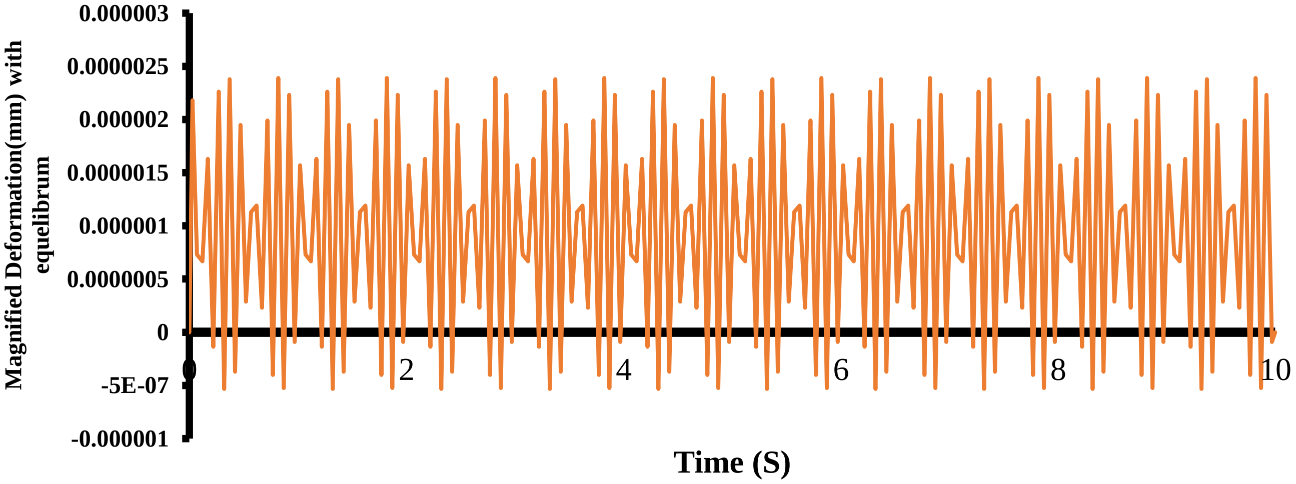

Fig. 10. Magnified directional deformation of the cylinder drum under applied dynamic load

The relationship between time and the magnified deformation of the cylindrical drum under a dynamic load of 942.78 N is depicted in Figure (10). The results of the CAD model analysis were recorded using ANSYS 2023 R1 software. The y-axis displays the magnified deformation value in millimeters, with values ranging from 0 mm to around 0.000003 mm. The x-axis depicts time in seconds, ranging from 0 to 10 seconds. The material's instantaneous reaction to dynamic stress is demonstrated by the initial, fast rise in deformation that occurs when the load is first applied on the blade, getting 2.39×10^{-6} mm. A stabilization period ensues, during which the deformation achieves equilibrium under the applied load. The cylindrical drum's greatest recorded deformation indicates how much it has distorted as a result of this dynamic load. Critical information on the material's mechanical characteristics, such as its elasticity and yield strength, which are crucial for engineering applications, can be gained by analyzing these results. Design concerns are informed by knowledge of how materials respond to dynamic loads, ensuring that structures can sustain anticipated stress without suffering from excessive deformation or failure.

The drum's maximum displacement under operating load was estimated to be around 1.196 mm, demonstrating that the structure stays within allowable deformation bounds and maintains its integrity while in use. The stiffness values were determined to be 1.86×10^{8} N m^{-1} for the drum and 1.07×10^{8} N m^{-1} for the decorticator blade, showing that both parts are sufficiently rigid to bear applied forces without buckling or deforming too much.

The drum's damping coefficient of 186,000.65 Ns m^{-1} and the blade's damping coefficient of 107,000.2 Ns m^{-1} indicate excellent energy dissipation, reducing vibrational response while in use and extending the machinery's lifespan. Furthermore, the design's safety factor of 1.25 confirms its dependability under normal operating settings by reflecting a reasonable margin against potential failures. According to these findings, the breastplate and cylinder drum are both suitable for the dynamic stresses that are encountered during processing and are hence well suited for their intended uses. It is advised that these components be periodically inspected and monitored in order to handle any unexpected problems that might occur during extended operation. Overall, this research demonstrates the design's structural soundness and practicality of operation.

Table 5- The performance of the modified integrated machine compared to the existing machine

Machine	**Operation speed (rpm)**	**Clearance (mm)**	**Power consumption (L h^{-1})**	**Efficiency (%)**	**Output quality**	**Loss**	**Damage to fiber (%)**	**Capacity (kg h^{-1})**
Combined decorticating & corm grating machine	880	1-4	1.4	94.6	Very high	5.4 %	3.4	1543.5
Engine driven Warqe EnseteVentricosum	1050	1-6	1.2	92	High	8%	6	315-615
Design improvement and analysis of kocho, bulla, and fiber production machine	650-1050	< 2 and > 2	1.3	86.5-93.12	Medium	0.83 kg	10.16-1.92	57.63
Fiber decorticator	860	1-3	1.1	94	High	0.54 kg	3.5	978
Fuel-powered decorticator	950	1-6	1.1	93-96	High	0.6 kg	6	565
Corn granting machine	2,200	5×5 sieve	1.3	98	Very high	2%	No	1048.3
Stainless steel decorticating machine	950 - 1050	1-2	1.2	97	Very high	3%	4-2.5	581
Modified and an integrated enset processing machine	864	1- 4	1.4	96	Very high	4 %	2.3	1643.5

The modified and integrated enset processing machine stands out for its excellent performance across several key factors. With an operation speed of 864 rpm, it provides a high efficiency of 96%, making it an ideal choice for large-scale operations where both speed and energy efficiency are critical. The machine maintains low fiber damage at 2.3% and losses at 4%, which makes it one of the better options when it comes to preserving the quality of the processed material. Additionally, it has a capacity of 1643.5 kg h^{-1}, which is comparable to the Combined Decorticating & Corm Grating Machine (also at 1543.5 kg h^{-1}) and positions it as a high-output machine in this comparison.

When compared with other machines, the Modified and Integrated Enset Processing Machine offers significant advantages. It has a similar capacity and efficiency to the Combined Decorticating & Corm Grating Machine but achieves a slightly higher fiber preservation rate (2.3% compared to 3.4% in the Combined Decorticating & Corm Grating Machine), making it more favorable in terms of product quality. When compared with the Engine Driven Warqe, which operates at a higher rpm (1050) but has a lower capacity (315-615 kg h^{-1}) and higher fiber damage (6%), the Modified and Integrated Enset Processing Machine is far superior in terms of throughput, efficiency, and fiber quality. Furthermore, the Design Improvement and Analysis of Kocho, Bulla, and Fiber Production Machine, despite a similar efficiency range (86.5%-93.12%), falls short in terms of both capacity (57.63 kg h^{-1}) and fiber damage (up to 10.16%), making it less competitive for large-scale processing.

Conclusion

Crucial conclusions include the maximum tension in the belt system, which was calculated to be 235.2 N, and the importance of component stiffness and safety factors in ensuring the machine's operational reliability. The analysis of the shafts shows that shaft 1, with its superior resistance to torsional deformation and high safety factor, is optimal for high-load applications, while the lighter shafts (2, 3, and 4) are more suited to lower-load scenarios but require careful monitoring to avoid failure. The cylinder drum and breastplate dynamic study highlights the significance of stiffness and energy dissipation. The drum's low deformation under load, coupled with its rigidity and damping qualities, validates its capacity to sustain dynamic loads without failing.

Both the drum and the breastplate function well under operating conditions, and the design's safety factor (S.F.) for all components is 1.25, ensuring that the components operate within safe limits. A safety factor above 1 indicates a margin of safety between the material's strength and the stress it experiences during operation. Important information about the performance of the cylinder drum is revealed by the examination and analysis of its rigid dynamics under applied load. The figure representing the deformation behavior demonstrates that when the load is first applied, the drum experiences a quick initial distortion. This is followed by a stabilized period during which the deformation achieves equilibrium. The cylinder drum exhibits very little deformation when in use, as seen by the magnified deformation values, which range from 0 mm to roughly 0.000003 mm, and the deformation of the blade was 2.39×10^{-6} mm. This indicates that both the material and design of the drum are highly effective in withstanding dynamic loads. The analysis demonstrates the drum's elasticity, yield strength, and structural integrity, demonstrating its capacity to remain stable under the pressures present in normal operating circumstances. The drum's long-term dependability is indicated by this little deformation. The Modified and Integrated Enset Processing Machine offers a balanced combination of high capacity, excellent efficiency, low fiber damage, and optimal performance, making it a more reliable and effective option when compared to many of the other machines listed in Table 4. Its performance in terms of both speed and quality preservation positions it as a top contender for large-scale enset processing operations.

Authors Contribution

Beka Adugna: Conceptualization, Experiment design and execution, Data analysis, Resource provision, Draft, Reviewing and Editing, and Proofreading.

Kishor Purushottam: Supervision, Conceptualization, Providing technical advice, Conducting research analysis, Resource allocation, Draft, Reviewing and Editing, and Visualization.

Moera Gutu: Resource allocation, Draft, Reviewing and Editing.

References

1. Adamiec-Wójcik, I., Brzozowska, L., & Drąg, Ł. (2015). An analysis of dynamics of risers during vessel motion by means of the rigid finite element method. *Ocean Engineering*, *106*, 102-114. https://doi.org/10.1016/j.oceaneng.2015.06.053
2. Ahangarnezhad, N., Najafi, G., & Jahanbakhshi, A. (2019). Determination of the physical and mechanical properties of a potato (the Agria variety) in order to mechanise the harvesting and post-harvesting operations. *Research in Agricultural Engineering*, *65*(2), 33-39. https://doi.org/10.17221/122/2017-RAE
3. Al-Omiri, M. K., Mahmoud, A. A., Rayyan, M. R., & Abu-Hammad, O. (2010). Fracture resistance of teeth restored with post-retained restorations: an overview. *Journal of Endodontics*, *36*(9), 1439-1449. https://doi.org/10.1016/j.joen.2010.06.005
4. Ambekar, M. S., & Shinde, S. S. (2019). Structural Analysis and Optimization of 'C'Frame of Mechanical Press. *International Research Journal of Engineering and Technology (IRJET)*, *6*, 56-2395.
5. Ambrus, A., Skadsem, H. J., & Mihai, R. G. (2018). Similarity analysis for downscaling a full size drill string to a laboratory scale test drilling rig. *International Conference on Offshore Mechanics and Arctic Engineering*, *51296*, V008T11A005. https://doi.org/10.1115/OMAE2018-77202
6. Aygören, S. M., & Türkdoğdu, H. (2024). Forces, Structures, and the Evolution of Natural and Artificial Forms. *SETSCI-Conference Proceedings*, *18*, 50-59. https://doi.org/10.36287/setsci.18.1.0050
7. Bechtel, S. E., Vohra, S., Jacob, K. I., & Carlson, C. D. (2000). The stretching and slipping of belts and fibers on pulleys. *Journal of Applied Mechanics*, *67*(1), 197-206. https://doi.org/10.1115/1.321164
8. Bekele, A. E., Lemu, H. G., & Jiru, M. G. (2022). Exploration of Mechanical Properties of Enset–Sisal Hybrid Polymer Composite. *Fibers*, *10*(2). https://doi.org/10.3390/fib10020014
9. Bello, S. K., Lamidi, S. B., & Oshinlaja, S. A. (2020). Design and fabrication of cassava grating machine. *International Journal of Advances in Scientific Research and Engineering (IJASRE)*, *6*(1), 162-167. https://doi.org/10.31695/IJASRE.2020.33915
10. Borrell, J. S., Goodwin, M., Blomme, G., Jacobsen, K., Wendawek, A. M., Gashu, D., Lulekal, E., Asfaw, Z., Demissew, S., & Wilkin, P. (2020). Enset-based agricultural systems in Ethiopia: A systematic review of production trends, agronomy, processing and the wider food security applications of a neglected banana relative. *Plants, People, Planet*, *2*(3), 212-228. https://doi.org/10.1002/ppp3.10084
11. Bruyère, M. (1965). Modern Solutions to Coupling and Transmission Problems of Aircraft Engines. *The Aeronautical Journal*, *69*(654), 365-379. https://doi.org/10.1017/S0001924000059248
12. Carlson, W. B., & McKean, J. D. (1955). Cylindrical pressure vessels: stress systems in plain cylindrical shells and in plain and pierced drumheads. *Proceedings of the Institution of*

Mechanical Engineers, *169*(1), 269-293. https://doi.org/10.1243/PIME_PROC_1955_169_039_02
13. Chen, W., Cao, G., Yuan, D., Ding, Y., Zhu, J., & Chen, X. (2023). Study on Agricultural Machinery-Load-Testing Technology and Equipment Based on Six-Dimensional Force Sensor. In *Agriculture*, *13*(9). https://doi.org/10.3390/agriculture13091649
14. Chopra, A. K. (2021). Modal combination rules in response spectrum analysis: Early history. *Earthquake Engineering & Structural Dynamics*, *50*(2), 260-269. https://doi.org/10.1002/eqe.3333
15. Colledani, M., Tolio, T., Fischer, A., Iung, B., Lanza, G., Schmitt, R., & Váncza, J. (2014). Design and management of manufacturing systems for production quality. *Cirp Annals*, *63*(2), 773-796. https://doi.org/10.1016/j.cirp.2014.05.002
16. David Müzel, S., Bonhin, E. P., Guimarães, N. M., & Guidi, E. S. (2020). Application of the finite element method in the analysis of composite materials: A review. *Polymers*, *12*(4), 818. https://doi.org/10.3390/polym12040818
17. De Felice, A., & Sorrentino, S. (2019). On the dynamic behaviour of rotating shafts under combined axial and torsional loads. *Meccanica*, *54*(7), 1029-1055. https://doi.org/10.1007/s11012-019-00987-4
18. Deressa, A. A., Derese, G. K., & Dula, M. W. (2023). Pre-extension demonstration and evaluation of enset processing technologies in selected districts of west Shewa and southwest Shewa zones, Oromia, Ethiopia. *Journal of Science & Development (JSD)*, *11*(1), P61.
19. Digvijay, D. P., & Kiran, M. N. (2015). Design and finite element analysis of rope drum and drum shaft for lifted material loading condition. *International Engineering Research Journal (IERJ)*, *Special*, *2*, 2034-2040. https://doi.org/10.3744/SNAK.2020.57.5.254
20. Duflou, J. R., Sutherland, J. W., Dornfeld, D., Herrmann, C., Jeswiet, J., Kara, S., Hauschild, M., & Kellens, K. (2012). Towards energy and resource efficient manufacturing: A processes and systems approach. *CIRP Annals*, *61*(2), 587-609. https://doi.org/10.1016/j.cirp.2012.05.002
21. Feng, R., & Young, B. (2013). Stress concentration factors of cold-formed stainless steel tubular X-joints. *Journal of Constructional Steel Research*, *91*, 26-41. https://doi.org/10.1016/j.jcsr.2013.08.012
22. Ham, S., & Bathe, K.-J. (2012). A finite element method enriched for wave propagation problems. *Computers & Structures*, *94*, 1-12. https://doi.org/10.1016/j.compstruc.2012.01.001
23. Hamming, R. (2012). *Numerical methods for scientists and engineers*. Courier Corporation.
24. Hollaway, L. C. (2010). A review of the present and future utilisation of FRP composites in the civil infrastructure with reference to their important in-service properties. *Construction and Building Materials*, *24*(12), 2419-2445. https://doi.org/10.1016/j.conbuildmat.2010.04.062
25. Hosseini, S. A. A., & Khadem, S. E. (2009). Free vibrations analysis of a rotating shaft with nonlinearities in curvature and inertia. *Mechanism and Machine Theory*, *44*(1), 272-288. https://doi.org/10.1016/j.mechmachtheory.2008.01.007
26. Huertas, A. C. M., Schmelzer, C. E. H., Hoehenwarter, W., Heyroth, F., & Heinz, A. (2016). Molecular-level insights into aging processes of skin elastin. *Biochimie*, *128*, 163-173. https://doi.org/10.1016/j.biochi.2016.08.010
27. Jäger, F. (2023). The Prince's Prosthetic Body: Orthopedic Armor and Material Self-Fashioning in Sixteenth-Century Europe. *The Art Bulletin*, *105*(3), 61-89. https://doi.org/10.1080/00043079.2023.2176666
28. Jemghili, R., Ait Taleb, A., & Mansouri, K. (2023). A collaborative multidisciplinary design methodology for additive manufacturing with a left-handed mouse as a case study. *The International Journal of Advanced Manufacturing Technology*, *125*(11), 4925-4951. https://doi.org/10.1007/s00170-023-11051-7
29. Jima, B. A., Kolhe, K. P., & Jiru, M. G. (2025). Design and development of an integrated enset

processing machine suitable for central highland farmers of west shewa zone Ethiopia. *Discover Agriculture*, *3*(1), 1. https://doi.org/10.1007/s44279-024-00114-2

30. Khodabakhshian, R., & Emadi, B. (2015). Development of a finite element method model to determine mechanical behavior of pumpkin seed. *International Journal of Food Properties*, *18*(2), 231-240. https://doi.org/10.1080/10942912.2013.822883
31. Khurmi, R. S., & Gupta, J. K. (2019). *A Textbook of Machine Design (LPSPE)*. S. Chand publishing.
32. Kordestani, M., Saif, M., Orchard, M. E., Razavi-Far, R., & Khorasani, K. (2019). Failure prognosis and applications—A survey of recent literature. *IEEE Transactions on Reliability*, *70*(2), 728-748. https://doi.org/10.1109/TR.2019.2930195
33. Kudama, G., Tolera, T., & Gebeyehu, L. (2022). Good farm practices and improved processing technology of enset for sustainable hunger solution in Ethiopia. *Journal of Innovation and Entrepreneurship*, *11*(1), 17. https://doi.org/10.1186/s13731-022-00210-x
34. Lemos, J. V. (2007). Discrete element modeling of masonry structures. *International Journal of Architectural Heritage*, *1*(2), 190-213. https://doi.org/10.1080/15583050601176868
35. Li, A., Pirrung, G. R., Gaunaa, M., Madsen, H. A., & Horcas, S. G. (2021). A computationally efficient engineering aerodynamic model for swept wind turbine blades. *Wind Energy Science Discussions*, *2021*, 1-49. https://doi.org/10.5194/wes-7-129-2022
36. Lu, Q., Li, C., Zhang, Y., Fang, H., & Bin, G. (2023). Study on the vibration control method of a turboshaft engine rotor based on piezoelectric squeeze film damper oil film clearance. *Mechanical Sciences*, *14*(1), 237-246. https://doi.org/10.5194/ms-14-237-2023
37. Mahmood, W., & Mohammed, A. (2022). Performance of ANN and M5P-tree to forecast the compressive strength of hand-mix cement-grouted sands modified with polymer using ASTM and BS standards and evaluate the outcomes using SI with OBJ assessments. *Neural Computing and Applications*, *34*(17), 15031-15051. https://doi.org/10.1007/s00521-022-07349-4
38. Mansfield, N., Naddeo, A., Frohriep, S., & Vink, P. (2020). Integrating and applying models of comfort. *Applied Ergonomics*, *82*, 102917. https://doi.org/10.1016/j.apergo.2019.102917
39. Mao, K. (2007). Gear tooth contact analysis and its application in the reduction of fatigue wear. *Wear*, *262*(11-12), 1281-1288. https://doi.org/10.1016/j.wear.2006.06.019
40. Mei, D., Zhao, X., Tang, G., Wang, J., Zhao, C., Li, C., & Wang, Y. (2022). A single-joint worm-like robot inspired by geomagnetic navigation. *Machines*, *10*(11), 1040. https://doi.org/10.3390/machines10111040
41. Mohanraj, R., Elangovan, S., Chandran, V. K., Sulaiman, M. F. M., Pradhaa, R. H., Poojasri, S., & Ramakrishna, J. R. (2021). Numerical analysis on bending and contact stress of single and double start worm drive. *Materials Today: Proceedings*, *46*, 8038-8044. https://doi.org/10.1016/j.matpr.2021.02.788
42. Murugan, S. S. (2020). Mechanical Properties of Materials: Definition, Testing and Application. *International Journal of Modern Studies in Mechanical Engineering (IJMSME)*, *6*(2), 28-38. https://doi.org/10.20431/2454-9711.0602003
43. Nabeshima, E. H., Moro, T. M. A., Campelo, P. H., Sant'Ana, A. S., & Clerici, M. T. P. S. (2020). Tubers and roots as a source of prebiotic fibers. In *Advances in food and nutrition research* (Vol. 94, pp. 267-293). Elsevier. https://doi.org/10.1016/bs.afnr.2020.06.005
44. O'Brien, D., Draper, S., & An, H. (2023). Stability of Concrete Mattresses. *International Conference on Offshore Mechanics and Arctic Engineering*, *86854*, V003T04A022. https://doi.org/10.1115/OMAE2023-106777
45. Olango, T. M., Tesfaye, B., Catellani, M., & Pè, M. E. (2014). Indigenous knowledge, use and on-farm management of enset (Ensete ventricosum (Welw.) Cheesman) diversity in Wolaita, Southern Ethiopia. *Journal of Ethnobiology and Ethnomedicine*, *10*, 1-18.

https://doi.org/10.1186/1746-4269-10-41

46. Radzevich, S. P. (2012). Practical Gear Design and Manufacture. *Second Edi. Boca Raton London New York: CRC Press Taylor & Francis Group*, 307-368.
47. Sidhu, C., & El-Sayegh, Z. (2024). Comparative Analysis of Non-Pneumatic Tire Spoke Designs for On-Road Applications: A Traction Force Perspective. *International Design Engineering Technical Conferences and Computers and Information in Engineering Conference*, *88339*, V001T01A002. https://doi.org/10.1115/DETC2024-145579
48. Silveira Velloso, N., Luis Gonçalves Costa, A., Rodrigues Magalhães, R., Lúcio Santos, F., & Tavares de Andrade, E. (2018). The Finite Element Method Applied to Agricultural Engineering: A Review. *Current Agriculture Research Journal*, *6*(3), 286-299. https://doi.org/10.12944/carj.6.3.08
49. Sinha, S. K., & Turner, K. E. (2011). Natural frequencies of a pre-twisted blade in a centrifugal force field. *Journal of Sound and Vibration*, *330*(11), 2655-2681. https://doi.org/10.1016/j.jsv.2010.12.017
50. Szabó, B., Actis, R., & Rusk, D. (2021). Validation test of a predictor of fatigue failure under biaxial out-of-phase loading conditions. *Computer Methods in Applied Mechanics and Engineering*, *378*, 113718. https://doi.org/10.1016/j.cma.2021.113718
51. Tezuka, A. (2006). *Finite Element and Finite Difference Methods BT - Springer Handbook of Materials Measurement Methods* (H. Czichos, T. Saito, & L. Smith (eds.); pp. 973–1000). Springer Berlin Heidelberg. https://doi.org/10.1007/978-3-540-30300-8_19
52. Upadhyay, B. D., Sonigra, S. S., & Daxini, S. D. (2021). Numerical analysis perspective in structural shape optimization: A review post 2000. *Advances in Engineering Software, 155*, 102992. https://doi.org/10.1016/j.advengsoft.2021.102992
53. Vullo, V., & Vullo, V. (2020). Worm gears. *Gears: Volume 1: Geometric and Kinematic Design*, 465-568. https://doi.org/10.1007/978-3-030-36502-8_11
54. Wang, Q., Huang, P., & Yin, Y. (2021). Design and optimization of rolling mills pass based on parameterization and orthogonal test. *The International Journal of Advanced Manufacturing Technology*, *112*, 803-818. https://doi.org/10.1007/s00170-020-06353-z
55. Workesa, M., Gebresenbet, G., Fanta, A., & Chaka, A. (2021). Design and Development of Engine Driven Warqe (Ensete Ventricosum) Decorticating Machine. *American Journal of Mechanical and Industrial Engineering*, *6*(2), 17-27. https://doi.org/10.11648/j.ajmie.20210602.11
56. Wu, Y.-R., & Hsu, W.-H. (2014). A general mathematical model for continuous generating machining of screw rotors with worm-shaped tools. *Applied Mathematical Modelling*, *38*(1), 28-37. https://doi.org/10.1016/j.apm.2013.05.056
57. Xing, Y., Qin, M., & Guo, J. (2017). A Time Finite Element Method Based on the Differential Quadrature Rule and Hamilton's Variational Principle. In *Applied Sciences* (Vol. 7, Issue 2). https://doi.org/10.3390/app7020138
58. Yakoob Pasha, M., Devi, M. T., & Maheswari, T. S. U. (2024). Reliability Analysis of the Shaft Subjected to Twisting Moment and Bending Moment for The Exponential and Weibull Distributed Strength and Stress. *Indian Journal of Science and Technology*, *17*(6), 494-502. https://doi.org/10.17485/IJST/v17i6.1806
59. Yang, J., Zeng, H., Zhu, T., & An, Q. (2017). Study on the dynamic performance of concrete mixer's mixing drum. *Mechanical Sciences*, *8*(1), 165-178. https://doi.org/10.5194/ms-8-165-2017
60. Yang, T., Ma, H., Qin, Z., Guan, H., & Xiong, Q. (2022). Coupling vibration characteristics of the shaft-disk-drum rotor system with bolted joints. *Mechanical Systems and Signal Processing*, *169*, 108747. https://doi.org/10.1016/j.ymssp.2021.108747
61. Yeh, T.-J., & Wu, F.-K. (2009). Modeling and robust control of worm-gear driven systems.

Simulation Modelling Practice and Theory, *17*(5), 767-777. https://doi.org/10.1016/j.simpat.2009.01.002

62. Yemataw, Z., Chala, A., Ambachew, D., Studholme, D. J., Grant, M. R., & Tesfaye, K. (2017). Morphological variation and inter-relationships of quantitative traits in enset (Ensete ventricosum (welw.) cheesman) germplasm from south and south-western Ethiopia. *Plants*, *6*(4), 1-16. https://doi.org/10.3390/plants6040056
63. Zewdie, A. (2012). *Assessment of performance and adoption of improved enset processing technologies*. University of Applied science Va Hal Larensten.

بهبود و تحلیل اجزای دستگاه یکپارچه فرآوری محصول Enset با نام علمی *Ensete ventricosum*

بِکا آدوگنا[1]، کی‌شور پوروشُتام کوله[2*]، موئرا گوتو[1]

تاریخ دریافت: ۱۴۰۳/۱۱/۰۳
تاریخ پذیرش: ۱۴۰۳/۱۲/۲۶

چکیده

این پژوهش با هدف بهبود طراحی و عملکرد دستگاه یکپارچه فرآوری Enset انجام شد و تمرکز آن بر روی اجزای کلیدی مانند شفت، درام استوانه‌ای، صفحه محافظ (بِرِست‌پلیت) و تیغه درام بود. دستگاه‌های موجود فرآوری Enset به دلیل فرسودگی قطعات، خرابی‌های مکانیکی و طراحی نامناسب با ناکارآمدی‌هایی مواجه هستند که منجر به چالش‌های عملیاتی می‌شود. برای رفع این مشکلات، اصلاحات هدفمند در طراحی قطعات دستگاه برنامه‌ریزی شد. مواد مورد استفاده برای این قطعات بر اساس استانداردهای ASTM انتخاب گردید. قطعات اصلاح‌شده با استفاده از روش اجزای محدود در ماژول ورک‌بنچ نرم‌افزار ANSYS 2023 R1 در دانشگاه علوم و فناوری آداما، اتیوپی، به‌طور دقیق تحلیل شدند. نتایج مطالعه نشان داد که حداکثر تنش‌ها برای شفت، درام استوانه‌ای، تیغه و صفحه محافظ به‌ترتیب برابر با ۱۲۰، ۲۵۰، ۴۰۰ و ۲۶۰ مگاپاسکال و حداقل تنش‌ها به‌ترتیب ۳۰، ۷۰، ۱۲۰ و ۸۰ مگاپاسکال بودند. بیشترین تغییر شکل‌ها نیز به‌ترتیب ۰/۱۵، ۰/۳، ۰/۵۵ و ۰/۳۵ میلی‌متر گزارش شد و ضریب ایمنی بیشینه برای همه قطعات برابر با ۱۵ بود. این نتایج نشان می‌دهد که اصلاحات انجام شده شرایط کاری ایمن را فراهم می‌کند. طراحی به گونه‌ای است که درام، تیغه درام و صفحه محافظ سختی کافی برای تحمل نیروهای عملیاتی را دارند و تغییر شکل حداقلی (۶– ۱۰ * ۲/۳۹ میلی‌متر برای تیغه درام) در محدوده ضریب ایمنی ۱/۲۵ باقی می‌ماند. علاوه بر این، دستگاه عملکرد بسیار خوبی در جذب انرژی و پاسخ ارتعاشی از خود نشان داد که بیانگر استحکام ساختاری آن است.

واژه‌های کلیدی: تغییر شکل، تیغه درام، تنش، درام استوانه‌ای، صفحه محافظ، Enset

---

[1] گروه مهندسی مکانیک، دانشکده مهندسی مکانیک، شیمی و مواد، دانشگاه علوم و فناوری آداما، آداما، اتیوپی
[2] بخش مهندسی مکانیک، دانشکده مهندسی سینگهد، وادگاون (BK)، ۴۱۱۰۴۱، دانشگاه ساویتری‌بای‌فوله پونه، هند
(*- نویسنده مسئول: Email: kishorkolhe05@gmail.com)

https://doi.org/10.22067/jam.2025.91751.1334